applied optics

Complex refractive index of volcanic ash aerosol in the infrared, visible, and ultraviolet

Alexandre Deguine,[1,2,3,*] Denis Petitprez,[2] Lieven Clarisse,[3] Snævarr Guðmundsson,[4] Valeria Outes,[5] Gustavo Villarosa,[5] and Hervé Herbin[1]

[1]Univ. Lille, CNRS, UMR 8518—LOA—Laboratoire d'Optique Atmosphérique, F-59000 Lille, France
[2]Univ. Lille, CNRS, UMR 8522—PC2A—Laboratoire de Physicochimie des Processus de Combustion et de l'Atmosphère, F-59000 Lille, France
[3]Université Libre de Bruxelles (ULB), Service de Chimie Quantique et Photophysique, Atmospheric Spectroscopy, Brussels, Belgium
[4]Nature Research Center of Southeast Iceland, Höfn í Hornafirði, Iceland
[5]IPATEC, CONICET-Universidad Nacional del Comahue, Bariloche, Argentina
*Corresponding author: adeguine@ulb.ac.be

Received 18 September 2019; revised 21 November 2019; accepted 26 November 2019; posted 26 November 2019 (Doc. ID 378045); published 22 January 2020

Very fine silicate-rich volcanic ash, generated by explosive volcanic eruptions, can efficiently be traced downwind with infrared satellite sounders. Their measurements can also be used to derive physical parameters, such as optical depths and effective radii. However, one of the key requirements for accurate retrievals is a good knowledge of the complex refractive index (CRI) of the ash under investigation. In the past, the vast majority of the studies used the CRIs from Pollack *et al.* [Icarus 19, 372 (1973)], which are based on measurements of thin slices of volcanic rock, and therefore are not representative for airborne volcanic ash particles. Here, we report measurements of the CRI of volcanic ash in suspension, generated from samples collected from recent high-impact eruptions in Chile (Puyehue-Cordón Caulle, Calbuco, and Chaitén), Iceland (Eyjafjallajökull and Grímsvötn), and Italy (Etna). The samples cover a wide range of SiO_2 content (46% to 76%) as confirmed by an X-ray fluorescence analysis. In the experimental setup, volcanic ash was suspended in nitrogen through mechanical agitation. Extinction spectra were recorded in the infrared, visible, and ultraviolet spectral regions. The particle size distribution within the airflow was also recorded. An iterative algorithm allowed us to obtain fully consistent CRIs for the six samples, compatible with the observed extinction spectra and the Kramers–Krönig relations. While a good agreement is found with other recently reported CRIs in the UV/Vis, larger differences are found in the longwave infrared spectral region.

https://doi.org/10.1364/AO.59.000884

1. INTRODUCTION

Huge quantities of silicate-rich aerosols are generated and ejected into the atmosphere during an explosive volcanic eruption. In the proximity of the volcano, ash can have a dramatic effect on infrastructure, human health and agriculture [1,2]. Very fine (< 32 μm) ash, which can be transported in the atmosphere over long distances, poses a significant risk to aviation, as ash can damage cockpit windows and clog aircraft engines [3–6]. The potential impact of volcanic particles on aviation was highlighted in April and May 2010 when a large part of the European airspace was closed for several days following the eruption of the Eyjafjallajökull volcano in Iceland [7–10]. The total financial impact of the event was estimated at 5 billion euros [11]. This event underlined the need to improve near-real time observations and forecasts of volcanic eruptions and ash clouds [12,13].

Satellite observations are the only practical way that volcanic ash clouds can be tracked over long distances. On the one hand, there are instruments that measure in the ultraviolet/visible (UV/Vis) spectral range. While they are relatively sensitive to volcanic aerosol [14], they are less sensitive to the size and chemical composition of particles. In addition, they only operate in the presence of sunlight, and are therefore not suitable for continuous near-real time monitoring. Thermal infrared (TIR) sounders, on the other hand, do not have this limitation. Thanks to a characteristic absorption band around 10 μm, they are very sensitive to fine volcanic ash, and can differentiate volcanic ash from clouds and other aerosol [15–17]. Fortunately, there are currently a myriad of polar and geostationary infrared sounders in orbit, which together allow efficient detection and tracking of volcanic clouds [18,19]. Exploiting the variations in absorption and scattering coefficients in the 7.5–12.5 μm spectral range, infrared sounders can also quantify a series of

physical properties of the observed ash, such as effective radii, optical depths, mass, altitude, and even composition, all with varying degrees of confidence [17,20–24]. Knowledge of these properties can not only help forecast the movement and fate of a volcanic plume in real time, but can also improve our capability to model volcanic plumes in the future [25]. However, the key parameter on which all satellite retrievals depend is the CRI, which links together the microphysical and optical properties. With the help of the CRI of ash, synthetic satellite spectra can be simulated (with a so-called forward model), and actual observed spectra can be analyzed to retrieve physical parameters (with an inverse model).

The majority of satellite studies that report measurements of volcanic ash currently rely on CRI measurements made in the 1970s on bulk material [26,27,28]. It is well-known, however, that such measurements underestimate the contribution of scattering in aerosol [29–31]. In addition, it has been shown that the spectra observed by satellites cannot be reproduced by forward models relying on these indices, especially when the optical depth is large [32]. This issue casts further doubt on the reliability of retrievals using these same indices. Measurements of CRIs of aerosol in suspension (not necessarily on volcanic ash) are becoming more commonplace [33]. Previously published refractive indices of volcanic ash in the infrared are listed in Table 1. Here, we build upon the work of Refs. [30,36] and present the CRIs of volcanic ash in suspension, generated from samples collected from recent high-impact eruptions in Chile (Puyehue-Cordón Caulle, Calbuco, and Chaitén), Iceland (Eyjafjallajökull and Grímsvötn) and Italy (Etna).

The six different volcanic ash samples are presented in the next section, together with the results of an X-ray fluorescence (XRF) analysis of their chemical composition. Section 3 describes the experimental setup employed and optimized in this study, consisting of a closed air circuit including a mechanical suspension device, two separate spectrometers (in the IR and UV/Vis range), and an aerodynamic particle sizer (APS). The setup has been detailed and validated in a previous study [36], so here we give a summary of its main features, and present the measured extinction spectra of the six samples. The newly retrieved refractive indices are presented in Section 4, after a summary has been given of the iterative retrieval procedure, which converts the measured extinction spectra into CRIs. Until now, only Reed *et al.* (2018) [34] has provided CRIs of volcanic ash in suspension. We compare our results with those results, and the historically important 1973 measurements of Pollack *et al.* [26]. We conclude this paper with a summary and directions for future work.

2. ASH SAMPLES

Because the primary interest in the optical properties of volcanic ash is for remote sensing applications, the samples were selected from recent eruptions for which large (long-lived) ash plumes were observed from space [17]. The selection was made to encompass a large range of ash types, as shown in Fig. 1. This figure gives an overview of the samples in the Total Alkali Silica diagram (TAS) [37]; samples from other studies for which refractive indices are available in the infrared are also included in Table 1. Two samples of rhyolitic ash were selected, as the widely used refractive indices of obsidian [26] are known to be largely inadequate [32]. These samples are from the 2011 Puyehue-Cordón Caulle eruption [16,38–40] and the 2008 Chaitén eruption [41–43]. Samples were also taken from the 2010 Eyjafjallajökull [44,45] and 2015 Calbuco eruptions [46,47]; both had a significant (societal) impact and produced ash with intermediate SiO_2 concentrations. The 2011 Grímsvötn and 2017 Etna samples were selected because of their basaltic composition; the former is also very well documented [48–51].

Table 1. Overview of Complex Refractive Indices of Volcanic Ash and Igneous Volcanic Rocks Retrieved in the Infrared Spectral Region[a]

Sample	Refractive Index	Spectral Range (μm)	Sampling Analysis	Reference
Askja	n, k	0.33–19	Suspension	[34]
Calbuco	n, k	00.31–1, 3.33–14.49	Suspension	This study
Chaitén	n, k	0.31–1, 3.33–14.49	Suspension	This study
Etna	n, k	0.31–1, 3.33–14.49	Suspension	This study
Eyjafjallajökull	n, k	0.33–19	Suspension	[34]
	n, k	0.34–1.04, 3.33–14.49	Suspension	This study
Grímsvötn	n, k	0.33–19	Suspension	[34]
	n, k	0.31–1, 3.33–14.49	Suspension	This study
Mayon	k	1–20	Pellet	[35]
Mt. Aso	n, k	0.33–19	Suspension	[34]
Mt. Spurr	n, k	0.33–19	Suspension	[34]
Nisyros	n, k	0.33–19	Suspension	[34]
Puyehue-Cordón Caulle	n, k	0.31–1, 3.33–14.49	Suspension	This study
Tongariro	n, k	0.33–19	Suspension	[34]
Andesite	n, k	0.4–50	Bulk	[26]
Basalt	n, k	0.4–50	Bulk	[26]
Obsidian	n, k	0.21–40	Bulk	[26]
Pumice	n, k	0.2–40	Pellet	[27]

[a]For an overview of measurements in the UV/Vis range only, refer to [74]. Most of these are publicly available in the Aerosol Refractive Index Archive (ARIA) at http://eodg.atm.ox.ac.uk/ARIA/.

Information of the volcanic ash samples (sample date, date of eruption, sampling details, references), as well as their elemental composition is provided in Table 2. The major elements were determined by a semiquantitative X-ray fluorescence (XRF) analysis using a S4 Pioneer Bruker with an uncertainty of 3%. For the analysis, samples were deposited on a boric acid pellet and compressed at 8 tons. All ashes were very fine except those from Etna, which had to be crushed using a mortar before being deposited on the boric acid pellet. The composition of the different samples reported in Table 2 is in generally good agreement (typically within 2–3%) with those reported in the references. The only exception is Grímsvötn, for which reported SiO_2 contents vary from 46 to 54%.

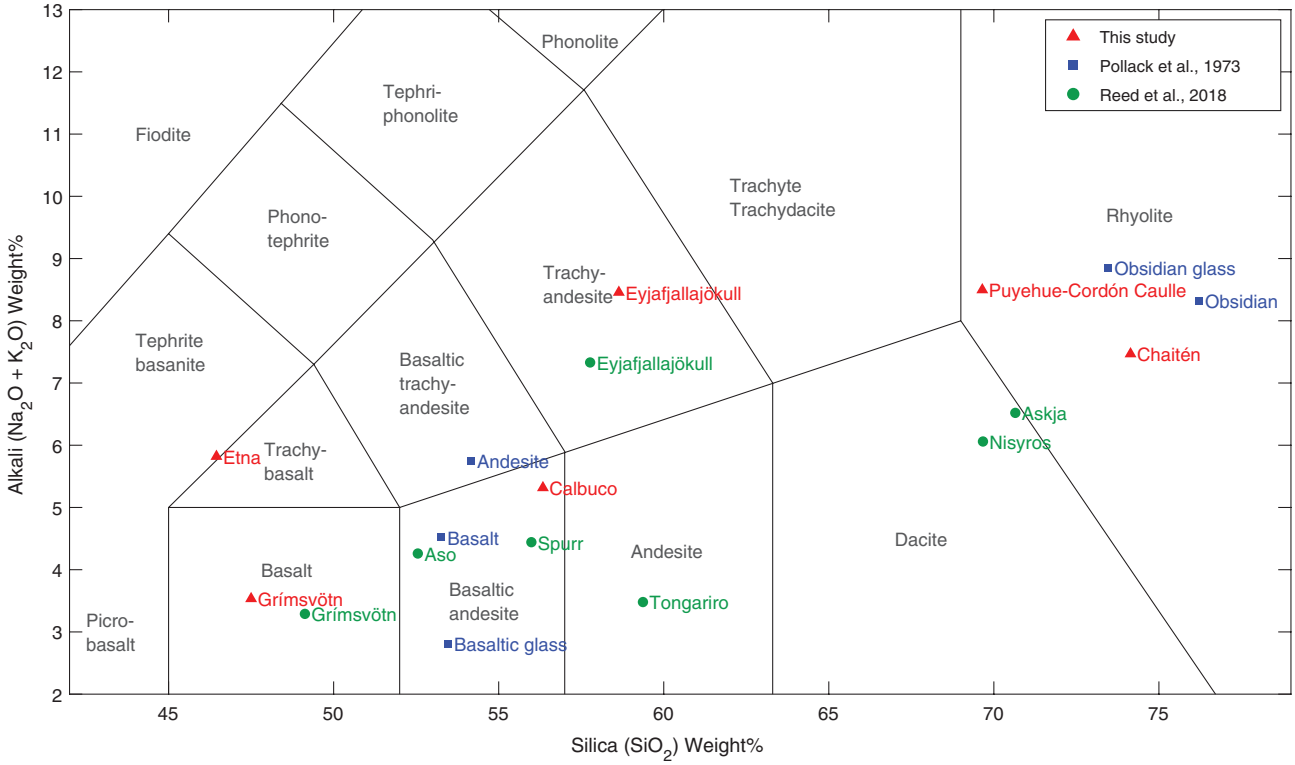

Fig. 1. TAS diagram with the ash samples measured in this study, and those of others for which refractive indices in the thermal infrared are available. The values for Spurr comes from Ref. [31].

Table 2. Volcanic Ash Samples and Their Major Elemental Composition Determined by an XRF Analysis (in Oxide Weight %)

Volcano Eruption Date	Type Sampling Date	Complementary Info	SiO_2	Al_2O_3	Na_2O	K_2O	Fe_2O_3	CaO	MgO	TiO_2	Ref.
Chaitén May 3, 2008	Rhyolite May 5, 2008	Direct fall, fresh ash, no rain, white, and fine	74.1	14.1	4.4	3.4	1.6	1.6	0.3	0.2	[41–43]
Puyehue-Cordón Caulle June 4, 2011	Rhyolite June 8, 2011	Ash deposit, no rain, white, and fine	69.7	14.1	5.5	3.2	4.1	2.0	0.4	0.6	[16,38–40]
Eyjafjallajökull May 4, 2010	Trachy-andesite June 13, 2012	Very fine, grey	58.6	15.4	6.1	2.4	8.8	4.8	1.7	1.4	[44,45]
Calbuco April 22, 2015	Basaltic-andesite April 23, 2015	Fresh ash, direct fall, fine, and brown	56.3	19.1	4.6	0.8	7.3	8.6	1.9	0.8	[46,47]
Grímsvötn May 21, 2011	Basalt May 22, 2011	Fine and dark	47.5	12.9	3.0	0.5	16.5	10.9	4.7	3.1	[48,49]
Etna March 16, 2017	Trachy-basalt Sept. 19, 2017	Very coarse and dark grey	46.5	17.8	3.8	2.0	11.4	11.7	4.1	1.8	[50,51]

3. EXPERIMENTAL SETUP AND MEASURED EXTINCTION SPECTRA

The experimental setup closely follows the one described in Ref. [36], where it was validated with calibrated amorphous silicon dioxide spherical particles (0.5 and 1 μm diameter, with a purity of 99.9% and a density of 1800 kg · m^{-3}). A photo of the experimental setup is shown in Fig. 2.

The first component of the setup is where aerosol is generated by mechanical agitation. It consists of a nitrogen inlet arriving into a glass tube, with the ash and a magnetic stirrer in the bottom. The nitrogen flow not only affects the particle concentration but also the deposition of particles on mirrors. For this reason, the flow was limited to 2 L · min^{-1}. The aerosol flux continues into a buffer volume, which helps produce an even and homogeneous cloud of aerosol from there into the spectrometers that record total extinction as a function of wavenumber. First in line is the Fourier transform infrared spectrometer, an Antaris IGS (Thermo Scientific) that measures the extinction from 690 to 3000 cm^{-1}. This spectrometer is composed of a multipass cell (white cell) with an optical length of 10 m; it is horizontally oriented to minimize the deposition of particles on mirrors. To overcome absorption of water vapor and carbon dioxide (CO_2) in the spectral range of the IR, the system

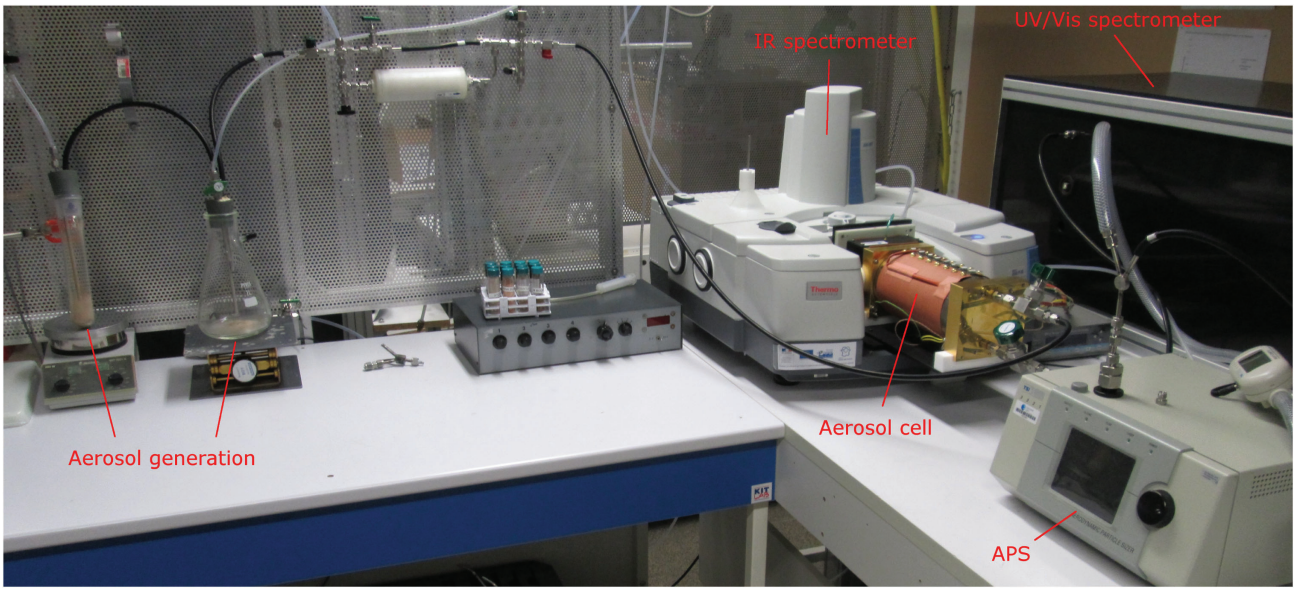

Fig. 2. Photo of the experimental setup. On the left, the ash is brought into suspension in a homogenous way. The flow then continues in the spectrometers, before reaching the APS that measures the size distribution of the particles in the flow.

is purged with nitrogen (N_2) for several hours before the experiment. This step is needed both for the Michelson interferometer and the multipass cell. For the UV/Vis part, an Ocean Optic Maya 2000-Pro spectrometer records the extinction spectra from 10000 to 32500 cm^{-1}. Compared to Ref. [36], a series of improvements have been implemented. A new single pass cell of 1 m optical path has been built, allowing the injection of volcanic ash at an angle of 45°. This reduces the impact of the flow and associated deposit of ash at the inlet and outlet of aerosol cells. Additionally, the internal diameter of the cell has been increased from 16 mm to 48 mm, increasing the cell volume, which helps the collimated beam avoid crossing the edges of the cell. To check the variability of the intensity of the source lamps, a second detector (Ocean Optics 2000+) was set up in parallel. This additional detector is directly connected to an optical fiber and records at the beginning of each experiment, the source intensity I_0, which might vary slowly in the course of several recordings.

The recorded extinction spectra $E = -\log_{10}(I/I_0)$ of the six volcanic ash samples are presented in Fig. 3 (gray lines). Especially in the UV/Vis spectral region, the signal measured by the spectrometer can exhibit significant levels of noise, due to small fluctuations of the source intensity. The spectra in the IR exhibit a dominant extinction feature in the region between 8 and 12 μm for the six different samples. These absorption bands are related to the vibration of $T-O^-$ bonds (where T refers to fourfold coordinated cations (Si^{4+}, Al^{4+}, Fe^{3+}) and O^- non-bridging oxygens (NBO)) [52]. Because the major component of volcanic ash is amorphous silicate, the main absorption band centered around 10 μm is due to the asymmetric stretching vibrations of Si-O-Si bridges. With increasing SiO_2 content, one can observe that (i) the absorption feature becomes narrower, (ii) a shoulder starts to appear around 9 μm (especially noticeable for Chaitén and Puyehue-Cordón Caulle), and (iii) the maximum is shifted toward higher wavenumbers. In this context also see [52–54]. A secondary maximum can be observed around 12.5 μm and is associated with symmetric vibrations of Si-O [53,55]. As noted by [52], the strength of this feature is closely related to the SiO_2 content, which is consistent with the fact that the feature is almost unnoticeable for the samples with the lowest SiO_2 content (Etna and Grimsvötn).

The slowly varying extinction in the UV/Vis spectral region is caused primarily by scattering. (As we will confirm further, the imaginary part of the CRI is close to zero in this region.) The most important information in the UV-Vis spectral region is contained between 10000 and 20000 cm^{-1}, where the maximum is observed. This maximum corresponds to the first maximum of the "interference structure," as also predicted by Mie theory [56,57]. Note that in this spectral region, source instability is a source of additional noise. Slight differences in the shape of the extinction spectra can be observed, such as a smaller dynamic range in the extinction for Eyjafjallajökull and a small feature around 0.55 μm in the spectrum of Puyehue-Cordón Caulle.

4. COMPLEX REFRACTIVE INDICES

A. Methodology

Complex refractive indices were retrieved from the measured extinction spectra using the optimal estimation method (OEM). The OEM is widely used in the remote sensing community to retrieve physical parameters from experimental measured spectra. We refer to Ref. [58] for detailed description of OEM and to Refs. [34,30,59] for applications of OEM in the context of the retrieval of refractive indices. In short, OEM is an iterative retrieval method, which in each loop improves the values of the physical parameters of interest (the so-called state vector) until convergence. In each iteration, a forward model is run with the current values to simulate the observations. Updated values are then obtained to improve the similarity between the measured and simulated observations,

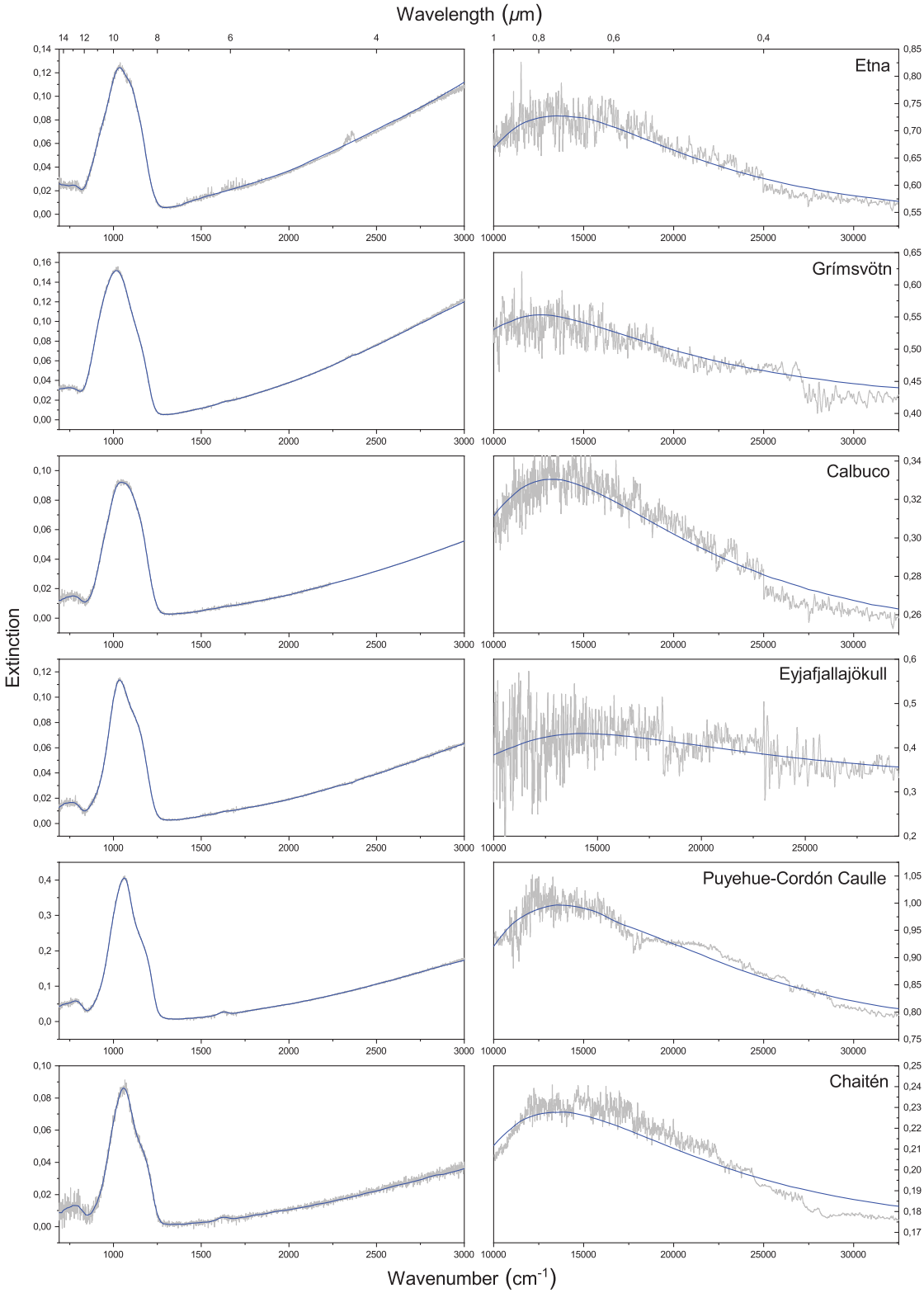

Fig. 3. Extinction spectra of the six volcanic ash samples: (in gray) the original extinction spectra recorded by spectrometers and (in blue) the spectra simulated at the end of the retrieval routine (from the Mie theory using the retrieved CRI).

while taking into account the a priori information. In our case, the state vector consists of the refractive indices and a set of parameters specifying the particle size distribution. The forward model consists of a standard Mie code [20]. In the next paragraphs we detail the state vector further, and then explain how the a priori data was gathered.

The real and imaginary parts of the CRI of a medium are related to each other via the Kramers–Krönig relations [60,61] as

$$n(\tilde{\nu}) - n_\infty = \frac{2}{\pi} P \int_0^\infty \frac{\tilde{\nu}' \kappa(\tilde{\nu}')}{\tilde{\nu}'^2 - \tilde{\nu}^2} \mathrm{d}\tilde{\nu}', \quad (1)$$

with $\kappa(\tilde{\nu}')$, the imaginary part of the CRI at the specific wavenumber $\tilde{\nu}'$, and P the Cauchy principal value. Relying on this equation, it thus suffices to retrieve the imaginary part κ of the CRI and an anchor point n_∞. The resulting CRI are immediately self-consistent, which cannot be guaranteed if both components are retrieved independently. The only caveat is that the numerical evaluation of the integral requires inter-and extrapolation of the refractive index outside the measurement intervals. Here we used a piecewise cubic Hermite interpolating polynomial and fixed values for the end points $\kappa_0 = \kappa_\infty = 0$. The choice was also made to retrieve the refractive indices at a coarser resolution than the measured extinction to avoid overfitting on the (noisy) data. In particular, in the LWIR the CRI was retrieved at a sampling of 5 cm^{-1}, increasing to $15 - 40$ cm^{-1} in the MWIR. In the UV/Vis spectral region, the resolution was set to 500 cm^{-1}, since the CRI only varies very slowly in this range. For the size distribution, a lognormal parameterization was chosen, with three parameters specifying the distribution: the total particle count N (particle $\cdot$ cm^{-3}), the geometric radius r_g, and the geometric standard deviation σ. Figure 4 shows the size distribution of the six samples fitted with lognormal functions that are frequently used to characterize the size distribution of volcanic ash [62]. It has also been the distribution of choice for in situ measurements [63–65]. Finally, the complete state vector consists of 228 variables on the CRI and three on the size distribution.

The a priori in the optimal estimation framework includes an a priori state vector (x_a) and an associated covariance matrix S_a. Together, these characterize the normal joint probability distribution of the parameters. For our retrieval, the covariance matrix was chosen to be entirely diagonal, as the retrieved parameters were chosen to be independent. We relied on the existing measurements of the CRI of igneous volcanic rocks and suspended ash to build an a priori of the imaginary part κ of the CRI. The a priori is shown in Fig. 5 and was obtained as the average of six CRIs: basalt, andesite, and obsidian from Ref. [26], and Grímsvötn, Eyjafjallajökull, and Nisyros from Ref. [34]. The same a priori was used for all the samples.

The UV/Vis part of the spectrum contains information on the anchor point n_∞. It is known [30] that the wavelength at which the maximum extinction occurs (see also what was said in Section 3 on the interference structure) is sensitive to the value of the real part of the CRI. For each measured extinction spectrum, an a priori value of the anchor point was obtained by manually adjusting its value to match the position of this maximum. For the ash from Eyjafjallajökull, the measured spectrum in the UV/Vis domain was, however, too noisy. For this sample, we

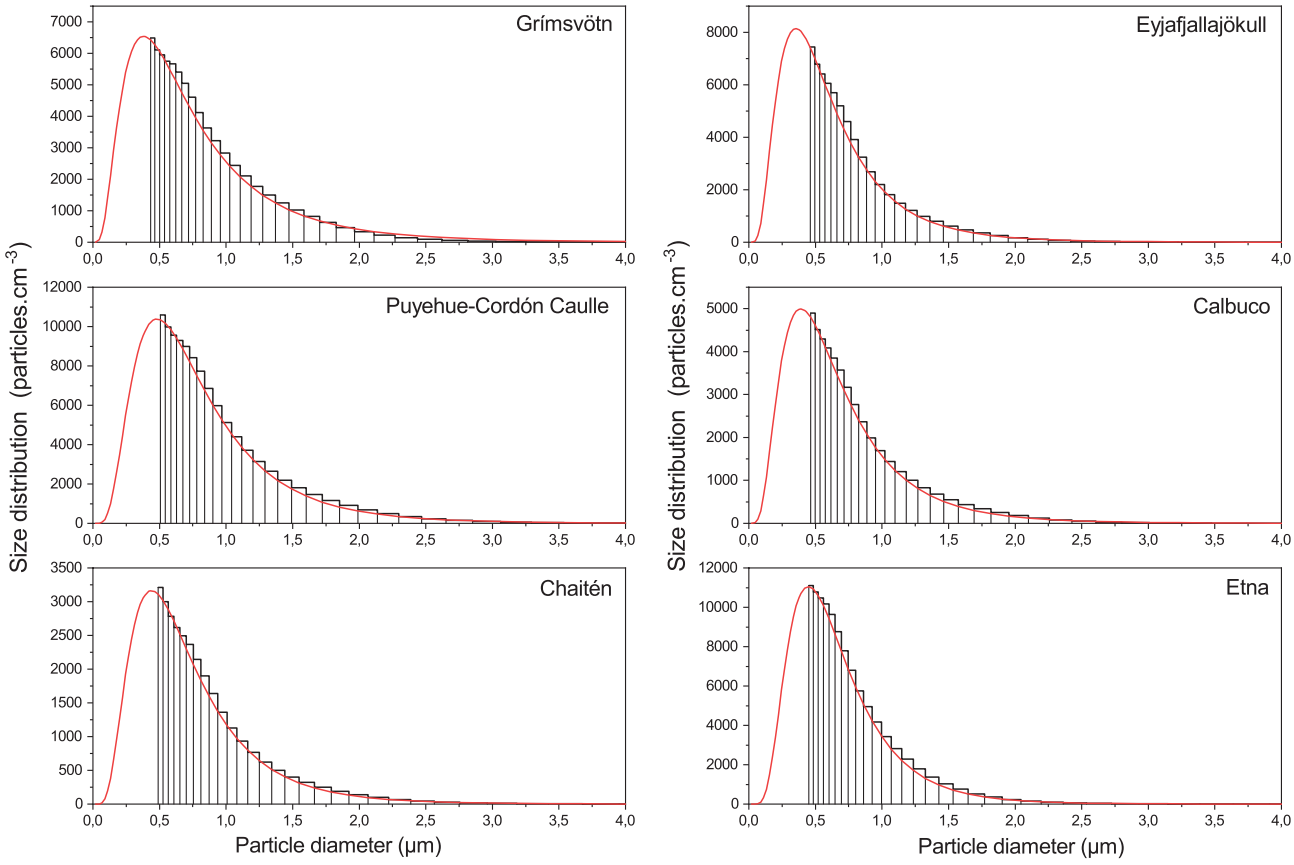

Fig. 4. Size distribution of the six volcanic ash samples fitted with lognormal function. Histograms represent the measured size distribution and red lines show the fit with lognormal function.

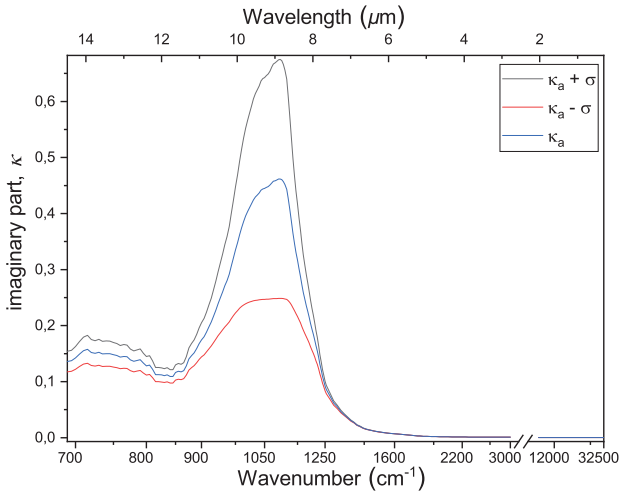

Fig. 5. A priori values of κ associated with the standard deviation.

used the empirical relation obtained in Ref. [31] between the real part of the CRI and the weight percent of SiO_2 to obtain the a priori value of the anchor point. In the next section we come back to this relation.

To estimate the impact of the a priori data on the retrieved CRIs, a series of tests were run with different choices for the a priori state vector. The results showed that the retrieved refractive indices were very similar to each other, as long as the variability in the covariance matrices was large enough. Typically, the extrema were almost at the same location, and the relative differences were maximally of the order of 0.1–0.2, which corresponds to around 10% at 1000 cm^{-1}.

The experimentally measured size distribution cannot be assumed to perfectly represent reality, as large uncertainties are associated with the APS measurements [66,67]. Nevertheless, a series of manipulations allowed us to use the size distribution recorded by the APS as an a priori. First, as the optical counters are less efficient at measuring small particles [66,68], we applied a correction using the empirical law derived in Ref. [69]. In addition, the size distribution measured by the APS is a function of the aerodynamic parameter (D_a) and not the geometrical diameter (D_g). To convert one into the other, we relied on

$$D_G = D_A\sqrt{\frac{\chi\rho_0}{\rho}}, \tag{2}$$

which is the formula given in Ref. [70], with ρ_0 the standard density ($1\ g\cdot cm^{-3}$) and ρ the particle density in $g\cdot cm^{-3}$. The particle densities were determined from the density of oxides [71], weighted with their fractional abundance, as measured by the XRF analysis. The dynamic shape factors χ were manually adjusted to yield a satisfactory fit in the UV/Vis part of the spectrum (tested values ranged from 1.1 to 1.82 [72,73]). The dynamic shape factor was set to a constant value of 1.82 for Chaitén, Puyehue-Cordón Caulle, and Eyjafjallajökull, and 1.64 for Etna, Calbuco, and Grímsvötn. After these corrections, the resulting size distribution was fitted to a lognormal function to obtain the a priori values for σ, N, and r_g.

In addition to a priori values, the optimal estimation retrieval also depends on constraints specified with covariance matrices. The a priori covariance matrix for κ was set to a constant diagonal value of 50% of the value of the a priori (see Fig. 5). As the anchor point is already estimated quite accurately prior to the OEM retrieval, its variance was set to 0.1%. For the size distribution we used variances of 10% for r_g, 20% for N, and 2% for σ. All the a priori information is summarized in Table 3 for each of the different samples.

A final parameter that must be specified for the OEM is the error covariance matrix. It defines to what extent we hope to approach the measured extinction spectra by the forward model. Again, this matrix was chosen diagonally and set to a value of 0.00005 in the infrared and 0.0002 in the UV/Vis spectral region. These values were chosen to be very small on purpose, to force the retrieval to find the best possible fit with the measured spectra. Alternatively, the variances of the a priori covariance matrices could have been increased, which would have achieved the same goal. The specific choices of the error and noise covariance matrices was obtained through experimentation. The values reported here allowed for adequate fits and, at the same time, yielded physically admissible retrieval parameters. To avoid nonphysical behavior of physical parameters fitted, a minimum value was set to 0 for all parameters. After each iteration the retrieved values were rounded to four digits.

The simulated extinction spectrum, obtained at the end of fit is shown in Fig. 3 (blue curve). In all cases it shows a very good agreement with the measured spectrum. Differences in the UV/Vis region are larger, but mostly within the instrumental noise.

B. Retrieved CRIs

The CRIs obtained using this retrieval procedure are shown in Fig. 6. In the thermal infrared, the real parts all have a large oscillation around 10 μm, and a corresponding local increase in the imaginary part, linked to vibrations of $T-O^{-1}$ bonds. The CRIs of the different samples are very variable, with the exception of samples that are closely located in the TAS diagram. The CRI of Etna and Grímsvötn, the samples with the lowest SiO_2 content (45–50%), exhibit the broadest, but flattest features, both in the real and the imaginary components. In addition,

Table 3. Parameters Composing the A Priori State Vector Associated with Their Variabilities

x_a	Chaitén	Puyehue-Cordón Caulle	Calbuco	Grímsvötn	Eyjafjallajökull	Etna	S_a (%)
κ	-	-	-	-	-	-	50
n_∞	1.51	1.51	1.61	1.61	1.58	1.63	0.1
N ($particle\cdot cm^{-3}\times 10^5$)	0.30	1.51	0.34	0.89	0.34	1.32	20
r_g (μm)	0.24	0.31	0.22	0.29	0.22	0.29	10
σ	1.80	1.62	1.75	1.66	1.74	1.58	2

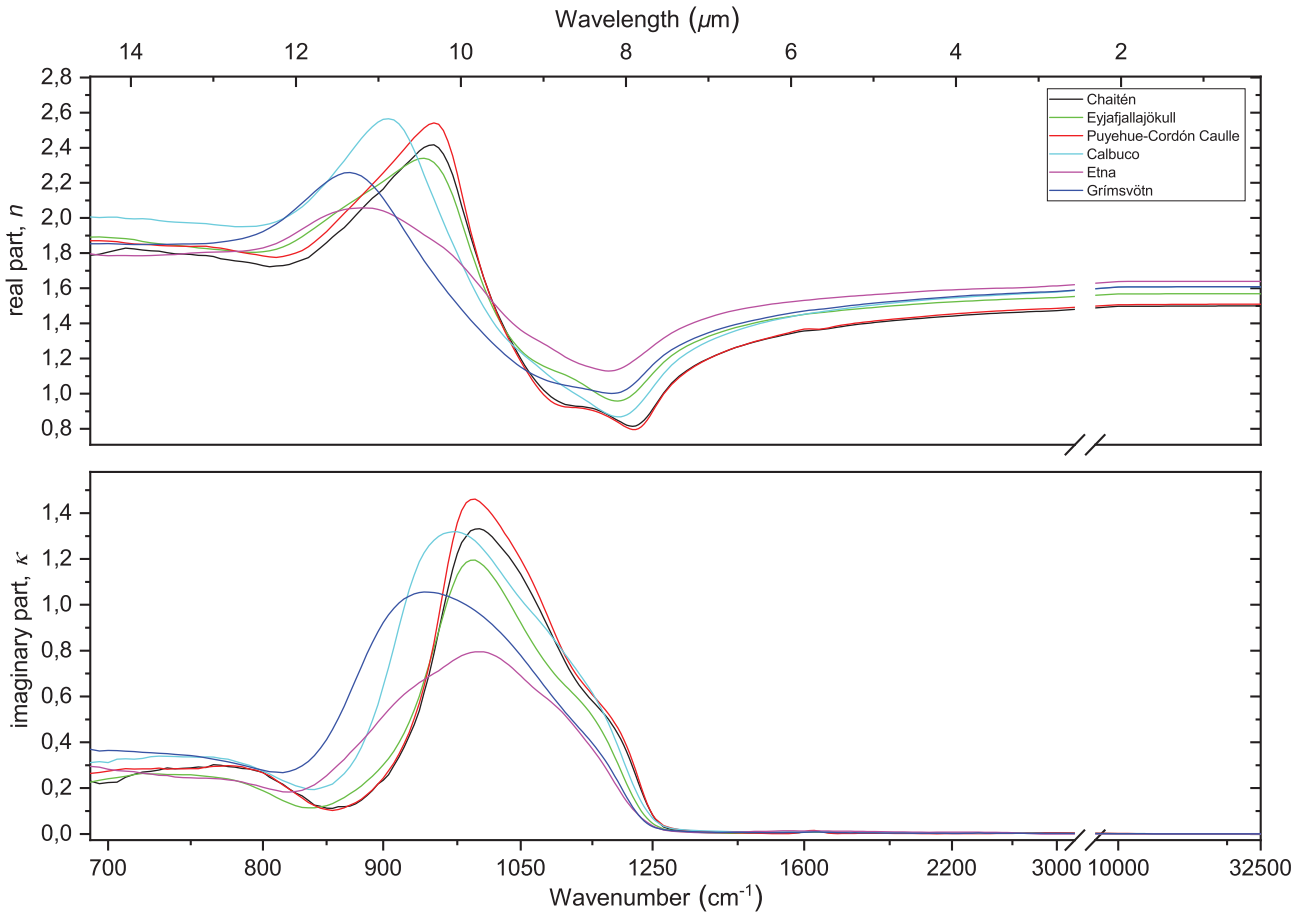

Fig. 6. Real and imaginary parts of the CRIs of the six volcanic ash samples. See supplementary material for underlying values.

the position at which n reaches its maxima is shifted toward longer wavelengths (around 11.5 μm), compared to the other samples. The CRI of the Chaitén and Puyehue-Cordón Caulle samples, had the highest SiO_2 content (67–75%), and represent the other extreme, with sharp and narrow features, and n and κ maxima shifted toward the lower wavelengths. The andesitic samples, Eyjafjallajökull and Calbuco, had an intermediary SiO_2 content, and corresponding CRI values in between the two extremes. Consistent with what we said before in the discussion of the extinction spectra, it is clear that the chemical composition of ash is strongly linked to these variations in the real and imaginary parts.

For the UV/Vis spectral region, the real and imaginary parts of the retrieved CRI do not present significant variations, with a value close to zero for the imaginary part and an almost constant value for the real part. A recent study [31] noted strong correlations between the SiO_2 content and the real and imaginary parts of the CRI from Ref. [34] at several wavelengths in the visible spectral region, with higher SiO_2 content associated with lower values of the real part of the CRI. Here, we were able to reproduce this result, as shown in Fig. 7, for the refractive index at 550 nm. The correlation coefficient of 0.94 is also in line with those found in that study. Note that we added a data point corresponding to the amorphous silica sample measured in Ref. [36].

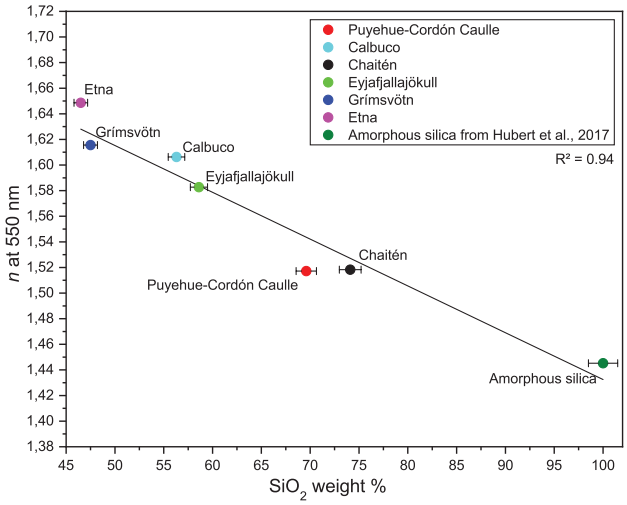

Fig. 7. Correlation between the real part of the CRI at 550 nm and the SiO_2 content.

C. Comparisons

In Fig. 8, the CRIs derived in this study are compared to those of the two other sets available: the historically important measurements from rock samples [26] and the more recent [34] from

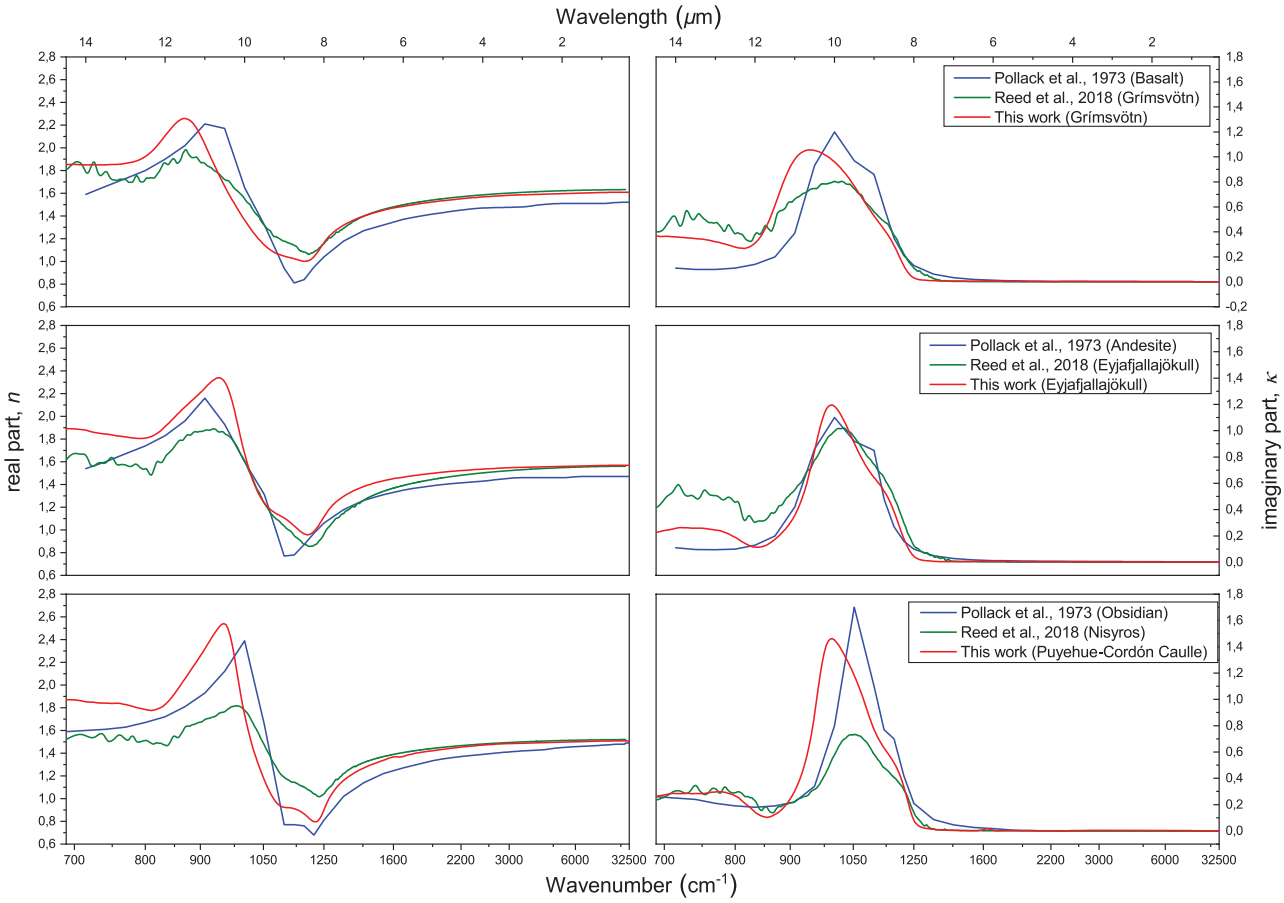

Fig. 8. Comparison of real and imaginary parts of CRIs from bulk material (blue, [26]), resuspended particles (green, [34]), and this study (red).

resuspended ash. To ease comparison, Fig. 8 shows just one representative for basaltic, andesitic, and rhyolitic ash (top, middle, and bottom panel) across the three datasets. A comparison of the CRIs of ash from the same eruption was only possible for Eyjafjallajökull and Grímsvötn ash, both reported here and in Ref. [34].

What was said before on the position of the n and κ maxima and the width of the features in the infrared is consistent with what is observed across the other two sets of measurement data. However, compared to the other two datasets, the maxima in the real parts (around 11 μm) are significantly larger and shifted toward the longer wavelengths for our indices. This shift is also seen in the imaginary part. This is particularly the case in comparison to Ref. [34], which reports significantly lower values in both the real and imaginary parts. For the rhyolitic ash samples, the maxima of the imaginary parts are different by almost a factor two. In this study, we used the Mie theory for the retrieval of the CRI, which is a theoretical model that is valid for a very wide range of particle sizes and wavenumbers, but which assumes spherical particles. In Ref. [34], the Rayleigh continuous distribution of ellipsoids (CDE) model was used. The CDE scattering model uses an assumed shape probability function corresponding to randomly oriented ellipsoids with the same volume. That model, however, is only valid when the size parameter x is smaller than one. (Refer to Ref. [56] for more details on CDE model.) In their setup, it was found to be able to better reproduce the CRI of silica. Figure 3 of Ref. [34] demonstrates that the use of this CDE model tends to produce CRIs with peak values shifted toward shorter wavelengths than when the Mie model is used. In addition, however, it appears that the CDE model leads to underestimated maximum values of n and κ [34]. Therefore, the differences with Ref. [34] that are observed in Fig. 8 seem to be largely due to the applied theoretical model.

For the UV/Vis part, the values found here are in excellent agreement with those reported in Ref. [34], and also with the dedicated UV/Vis measurements from Ref. [74]. The real parts of the indices in the UV/Vis part reported in Ref. [26] are, however, likely related to the fact that bulk measurements underestimate the contribution of scattering in aerosol.

5. CONCLUSION

Complex refractive indices have been retrieved in the thermal infrared ($690 - 3000\,\mathrm{cm}^{-1}$) and the visible-ultraviolet ($10000 - 32500\,\mathrm{cm}^{-1}$) spectral ranges for six volcanic ash samples. The samples were chosen from recent high-impact eruptions, and cover almost the entire range of SiO_2 fractions commonly found in volcanic ash. In the experimental setup, volcanic ash was mechanically made airborne, and extinction spectra and their particle size distributions were recorded in the two spectral ranges. The CRI were retrieved from extinction

spectra measured in the laboratory using an iterative procedure. In the UV/Vis, excellent agreement was found with previously reported measurements. However, differences with previously published indices are large in the infrared, with larger peak values in the real and imaginary components, and shifts toward longer wavelengths. In future studies, the research should assess whether remotely sensed spectra can be accurately simulated with the presented refractive indices, and to what extent retrieved remotely sensed quantities, such as particle radii and ash mass, are affected by the choice of the refractive index. The reported indices are available in the supplementary material (see Data File 1, Data File 2, Data File 3, Data File 4, Data File 5, Data File 6) and will be made available through the ARIA database.

Funding. Agence Nationale de la Recherche (ANR-11-LABX-0 0 05-01); Conseil Régional de Picardie; European Regional Development Fund; H2020 Societal Challenges (723986).

Acknowledgment. The CaPPA project (Chemical and Physical Properties of the Atmosphere) is funded by the French National Research Agency (ANR) through the PIA (Programme d'Investissement d'Avenir) under contract ANR-11-LABX-0 0 05-01 and by the Regional Council Nord Pas de Calais-Picardie and the European Funds for Regional Economic Development (FEDER). Part of this research was funded by the European Union's Horizon 2020 research programme for Societal Challenges - smart, green and integrated transport under grant agreement no. 723986 as part of the EUNADICS-AV project. The authors thank M. P. Delplancke and T. Segato of 4MAT, Ecole Polytechnique of the Université Libre de Bruxelles, for the XRF analysis; P. Hubert for his work on the experimental setup; and P.-F. Coheur for the Eyjafjallajökull ash sample. Lieven Clarisse is a research associate supported by the Belgian F.R.S–FNRS.

Disclosures. The authors declare that there are no conflicts of interest related to this paper.

REFERENCES

1. T. M. Wilson, C. Stewart, V. Sword-Daniels, G. S. Leonard, D. M. Johnston, J. W. Cole, J. Wardman, G. Wilson, and S. T. Barnard, "Volcanic ash impacts on critical infrastructure," Phys. Chem. Earth, Parts A/B/C **45–46**, 5–23 (2012).
2. P. J. Baxter and C. J. Horwell, "Impacts of eruptions on human health," in *The Encyclopedia of Volcanoes* (Elsevier, 2015), pp. 1035–1047.
3. M. Guffanti, T. J. Casadevall, and K. Budding, Encounters of Aircraft with Volcanic Ash Clouds; a Compilation of Known Incidents, 1953-2009, Data Series 545, ver. 1.0, 12 p., plus 4 appendices including the compilation database [https://pubs.usgs.gov/ds/545/] (U.S. Geological Survey, 2010).
4. M. Shinozaki, K. A. Roberts, B. van de Goor, and T. W. Clyne, "Deposition of ingested volcanic ash on surfaces in the turbine of a small jet engine," in *Advanced Engineering Materials* (2013), pp. 986–994.
5. J. Dean, C. Taltavull, and T. Clyne, "Influence of the composition and viscosity of volcanic ashes on their adhesion within gas turbine aero-engines," Acta Mater. **109**, 8–16 (2016).
6. T. J. Casadevall, P. Delos Reyes, and D. J. Schneider, "The 1991 Pinatubo eruptions and their effects on aircraft operations," in *Fire and Mud: Eruptions and Lahars of Mount Pinatubo*, C. G. Newhall and R. S. Punongbayan, eds. (Philippines Institute of Volcanology and Seismology/University of Washington, 1996), pp. 625–636.
7. A. Ansmann, M. Tesche, S. Groß, V. Freudenthaler, P. Seifert, A. Hiebsch, J. Schmidt, U. Wandinger, I. Mattis, D. Müller, and M. Wiegner, "The 16 April 2010 major volcanic ash plume over central Europe: EARLINET lidar and AERONET photometer observations at Leipzig and Munich, Germany," Geophys. Res. Lett. **37**, L13810 (2010).
8. A. R. Donovan and C. Oppenheimer, "The 2010 Eyjafjallajökull eruption and the reconstruction of geography," Geograph. J. **177**, 4–11 (2010).
9. M. T. Gudmundsson, R. Pedersen, K. Vogfjörd, B. Thorbjarnardóttir, S. Jakobsdóttir, and M. J. Roberts, "Eruptions of Eyjafjallajökull volcano, Iceland," Eos Trans. Am. Geophys. Union **91**, 190–191 (2010).
10. F. Sigmundsson and Á. Höskuldsson, "Develop instruments to monitor volcanic ash fallout," Nature **466**, 28 (2010).
11. Oxford Economics, "The economic impacts of air travel restrictions due to volcanic ash (report) (p. 12)," technical report (Abbey House, 2010).
12. C. Zehner, "Monitoring volcanic ash from space, ESA–EUMETSAT workshop on the 14 April to 23 May 2010 eruption at the Eyjafjöll volcano, south Iceland (ESA/ESRIN, 26–27 May 2010)," ESA Scientific & Technical Memoranda (2012).
13. S. Mackie, K. Cashman, H. Ricketts, A. Rust, and M. Watson, *Volcanic Ash: Hazard Observation* (Elsevier, 2016).
14. S. Carn and N. Krotkov, "Ultraviolet satellite measurements of volcanic ash," in *Volcanic Ash* (Elsevier, 2016), pp. 217–231.
15. L. Clarisse, F. Prata, J.-L. Lacour, D. Hurtmans, C. Clerbaux, and P.-F. Coheur, "A correlation method for volcanic ash detection using hyperspectral infrared measurements," Geophys. Res. Lett. **37**, L19806 (2010).
16. L. Clarisse, P.-F. Coheur, F. Prata, J. Hadji-Lazaro, D. Hurtmans, and C. Clerbaux, "A unified approach to infrared aerosol remote sensing and type specification," Atmos. Chem. Phys. **13**, 2195–2221 (2013).
17. L. Clarisse and F. Prata, "Infrared sounding of volcanic ash," in *Volcanic Ash* (Elsevier, 2016), pp. 189–215.
18. A. J. Prata, "Satellite detection of hazardous volcanic clouds and the risk to global air traffic," Nat. Hazards **51**, 303–324 (2009).
19. H. Brenot, N. Theys, L. Clarisse, J. van Geffen, J. van Gent, M. Van Roozendael, R. van der A, D. Hurtmans, P.-F. Coheur, C. Clerbaux, P. Valks, P. Hedelt, F. Prata, O. Rasson, K. Sievers, and C. Zehner, "Support to Aviation Control Service (SACS): an online service for near-real-time satellite monitoring of volcanic plumes," Nat. Hazards Earth Syst. Sci. **14**, 1099–1123 (2014).
20. L. Clarisse, D. Hurtmans, A. J. Prata, F. Karagulian, C. Clerbaux, M. D. Mazière, and P.-F. Coheur, "Retrieving radius, concentration, optical depth, and mass of different types of aerosols from high-resolution infrared nadir spectra," Appl. Opt. **49**, 3713–3722 (2010).
21. P. N. Francis, M. C. Cooke, and R. W. Saunders, "Retrieval of physical properties of volcanic ash using Meteosat: a case study from the 2010 Eyjafjallajökull eruption," J. Geophys. Res. **117**, D00U09 (2012).
22. A. J. Prata and A. T. Prata, "Eyjafjallajökull volcanic ash concentrations determined using spin enhanced visible and infrared imager measurements," J. Geophys. Res. **117**, D00U23 (2012).
23. A. Kylling, N. Kristiansen, A. Stohl, R. Buras-Schnell, C. Emde, and J. Gasteiger, "A model sensitivity study of the impact of clouds on satellite detection and retrieval of volcanic ash," Atmos. Meas. Tech. **8**, 1935–1949 (2015).
24. L. J. Ventress, G. McGarragh, E. Carboni, A. J. Smith, and R. G. Grainger, "Retrieval of ash properties from IASI measurements," Atmos. Meas. Tech. **9**, 5407–5422 (2016).
25. M. Gouhier, J. Eychenne, N. Azzaoui, A. Guillin, M. Deslandes, M. Poret, A. Costa, and P. Husson, "Low efficiency of large volcanic eruptions in transporting very fine ash into the atmosphere," Sci. Rep. **9**, 1449 (2019).
26. J. B. Pollack, O. B. Toon, and B. N. Khare, "Optical properties of some terrestrial rocks and glasses," Icarus **19**, 372–389 (1973).

27. F. E. Volz, "Infrared optical constants of ammonium sulfate, Sahara dust, volcanic pumice, and flyash," Appl. Opt. **12**, 564–568 (1973).
28. W. G. Egan, T. Hilgeman, and K. Pang, "Ultraviolet complex refractive index of Martian dust: Laboratory measurements of terrestrial analogs," Icarus **25**, 344–355 (1975).
29. C. D. Biagio, H. Boucher, S. Caquineau, S. Chevaillier, J. Cuesta, and P. Formenti, "Variability of the infrared complex refractive index of African mineral dust: experimental estimation and implications for radiative transfer and satellite remote sensing," Atmos. Chem. Phys. **14**, 11093–11116 (2014).
30. H. Herbin, O. Pujol, P. Hubert, and D. Petitprez, "New approach for the determination of aerosol refractive indices–Part I: theoretical bases and numerical methodology," J. Quantum Spectrosc. Radiat. Transfer **200**, 311–319 (2017).
31. G. S. Prata, L. J. Ventress, E. Carboni, T. A. Mather, R. G. Grainger, and D. M. Pyle, "A new parameterization of volcanic ash complex refractive index based on NBO/t and SiO_2 content," J. Geophys. Res. **124**, 1779–1797 (2019).
32. S. M. Newman, L. Clarisse, D. Hurtmans, F. Marenco, B. Johnson, K. Turnbull, S. Havemann, A. J. Baran, D. O'Sullivan, and J. Haywood, "A case study of observations of volcanic ash from the Eyjafjallajökull eruption: 2. airborne and satellite radiative measurements," J. Geophys. Res. **117**, D00U13 (2012).
33. R. Signorell and J. P. Reid, *Fundamentals and Applications in Aerosol Spectroscopy* (CRC Press, 2010).
34. B. E. Reed, D. M. Peters, R. McPheat, and R. G. Grainger, "The complex refractive index of volcanic ash aerosol retrieved from spectral mass extinction," J. Geophys. Res. **123**, 1339–1350 (2018).
35. E. M. Patterson, "Optical absorption coefficients of soil-aerosol particles and volcanic ash between 1 and 16 μm," in *Proceedings of the Second Conference on Atmospheric Radiation*, Washington, DC (American Meteorological Society, 1975), pp. 177–180.
36. P. Hubert, H. Herbin, N. Visez, O. Pujol, and D. Petitprez, "New approach for the determination of aerosol refractive indices–Part II: experimental set-up and application to amorphous silica particles," J. Quantum Spectrosc. Radiat. Transfer **200**, 320–327 (2017).
37. M. J. L. Bas, R. W. L. Maitre, A. Streckeisen, and B. Zanettin, "A chemical classification of volcanic rocks based on the total alkali-silica diagram," J. Petrol. **27**, 745–750 (1986).
38. E. Collini, M. S. Osores, A. Folch, J. G. Viramonte, G. Villarosa, and G. Salmuni, "Volcanic ash forecast during the June 2011 Cordón Caulle eruption," Nat. Hazards **66**, 389–412 (2012).
39. M. Elissondo, V. Baumann, C. Bonadonna, M. Pistolesi, R. Cioni, A. Bertagnini, S. Biass, J.-C. Herrero, and R. Gonzalez, "Chronology and impact of the 2011 Cordón Caulle eruption, Chile," Nat. Hazards Earth Syst. Sci. **16**, 675–704 (2016).
40. B. V. Alloway, N. J. G. Pearce, G. Villarosa, V. Outes, and P. I. Moreno, "Multiple melt bodies fed the AD 2011 eruption of Puyehue-Cordón Caulle, Chile," Sci. Rep. **5**, 17589 (2015).
41. G. Gangale, A. Prata, and L. Clarisse, "The infrared spectral signature of volcanic ash determined from high-spectral resolution satellite measurements," Remote Sens. Environ. **114**, 414–425 (2010).
42. A. J. Durant, G. Villarosa, W. I. Rose, P. Delmelle, A. J. Prata, and J. G. Viramonte, "Long-range volcanic ash transport and fallout during the 2008 eruption of Chaitén volcano, Chile," Phys. Chem. Earth, Parts A/B/C **45–46**, 50–64 (2012).
43. B. Alloway, N. Pearce, P. Moreno, G. Villarosa, I. Jara, R. De Pol-Holz, and V. Outes, "An 18, 000 year-long eruptive record from Volcán Chaitén, northwestern Patagonia: paleoenvironmental and hazard-assessment implications," Quat. Sci. Rev. **168**, 151–181 (2017).
44. M. T. Gudmundsson, T. Thordarson, Á. Höskuldsson, G. Larsen, H. Björnsson, F. J. Prata, B. Oddsson, E. Magnússon, T. Högnadóttir, G. N. Petersen, C. L. Hayward, J. A. Stevenson, and I. Jónsdóttir, "Ash generation and distribution from the April-May 2010 eruption of Eyjafjallajökull, Iceland," Sci. Rep. **2**, 572 (2012).
45. A. Stohl, A. J. Prata, S. Eckhardt, L. Clarisse, A. Durant, S. Henne, N. I. Kristiansen, A. Minikin, U. Schumann, P. Seibert, K. Stebel, H. E. Thomas, T. Thorsteinsson, K. Tørseth, and B. Weinzierl, "Determination of time and height resolved volcanic ash emissions and their use for quantitative ash dispersion modeling: the 2010 Eyjafjallajökull eruption," Atmos. Chem. Phys. **11**, 4333–4351 (2011).
46. J. Romero, D. Morgavi, F. Arzilli, R. Daga, A. Caselli, F. Reckziegel, J. Viramonte, J. Daz-Alvarado, M. Polacci, M. Burton, and D. Perugini, "Eruption dynamics of the 22-23 April 2015 Calbuco volcano (southern Chile): Analyses of tephra fall deposits," J. Volcanol. Geotherm. Res. **317**, 15–29 (2016).
47. F. Reckziegel, E. Bustos, L. Mingari, W. Báez, G. Villarosa, A. Folch, E. Collini, J. Viramonte, J. Romero, and S. Osores, "Forecasting volcanic ash dispersal and coeval resuspension during the April-May 2015 Calbuco eruption," J. Volcanol. Geotherm. Res. **321**, 44–57 (2016).
48. C. Horwell, P. Baxter, S. Hillman, J. Calkins, D. Damby, P. Delmelle, K. Donaldson, C. Dunster, B. Fubini, F. Kelly, J. L. Blond, K. Livi, F. Murphy, C. Nattrass, S. Sweeney, T. Tetley, T. Thordarson, and M. Tomatis, "Physicochemical and toxicological profiling of ash from the 2010 and 2011 eruptions of Eyjafjallajökull and Grímsvötn volcanoes, Iceland using a rapid respiratory hazard assessment protocol," Environ. Res. **127**, 63–73 (2013).
49. E. D. Moxnes, N. I. Kristiansen, A. Stohl, L. Clarisse, A. Durant, K. Weber, and A. Vogel, "Separation of ash and sulfur dioxide during the 2011 Grímsvötn eruption," J. Geophys. Res. **119**, 7477–7501 (2014).
50. A. Cappello, G. Ganci, G. Bilotta, A. Herault, V. Zago, and C. D. Negro, "Satellite-driven modeling approach for monitoring lava flow hazards during the 2017 Etna eruption," report (Istituto Nazionale di Geofisica e Vulcanologia, 2018).
51. M. Viccaro, M. Giuffrida, F. Zuccarello, M. Scandura, M. Palano, and S. Gresta, "Violent paroxysmal activity drives self-feeding magma replenishment at Mt. Etna," Sci. Rep. **9**, 6717 (2019).
52. D. D. Genova, D. Morgavi, K.-U. Hess, D. R. Neuville, N. Borovkov, D. Perugini, and D. B. Dingwell, "Approximate chemical analysis of volcanic glasses using Raman spectroscopy," J. Raman Spectrosc. **46**, 1235–1244 (2015).
53. G. Hunt, "Spectroscopic properties of rocks and minerals," in *Handbook of Physical Properties of Rocks*, R. Carmichael, ed. (CRC Press, 1982), pp. 295–385.
54. S. Scollo, G. A. Baratta, M. E. Palumbo, S. Corradini, G. Leto, and G. Strazzulla, "Linking the IR transmittance to size and type of volcanic ash particles," J. Geophys. Res. Atmos. **118**, 12207–12215 (2013).
55. R. Kitamura, L. Pilon, and M. Jonasz, "Optical constants of silica glass from extreme ultraviolet to far infrared at near room temperature," Appl. Opt. **46**, 8118–8133 (2007).
56. C. Bohren and D. Huffman, *Absorption and Scattering of Light by Small Particles* (Wiley, 1983).
57. H. C. V. D. Hulst, *Light Scattering by Small Particles* (Wiley, 1957).
58. C. D. Rodgers, *Inverse Methods for Atmospheric Sounding: Theory and Practice* (World Scientific, 2000), Vol. **2**.
59. G. E. Thomas, S. F. Bass, R. G. Grainger, and A. Lambert, "Retrieval of aerosol refractive index from extinction spectra with a damped harmonic-oscillator band model," Appl. Opt. **44**, 1332–1341 (2005).
60. V. Lucarini, J. J. Saarinen, K.-E. Peiponen, and E. M. Vartiainen, *Kramers–Kronig Relations in Optical Materials Research* (Springer Science & Business Media, 2005), Vol. **110**.
61. R. K. Ahrenkiel, "Modified Kramers–Kronig analysis of optical spectra," J. Opt. Soc. Am. **61**, 1651–1655 (1971).
62. K. H. Wohletz, M. F. Sheridan, and W. K. Brown, "Particle size distributions and the sequential fragmentation/transport theory applied to volcanic ash," J. Geophys. Res. [Solid Earth] **94**, 15703–15721 (1989).
63. B. Johnson, K. Turnbull, P. Brown, R. Burgess, J. Dorsey, A. J. Baran, H. Webster, J. Haywood, R. Cotton, Z. Ulanowski, E. Hesse, A. Woolley, and P. Rosenberg, "In situ observations of volcanic ash clouds from the FAAM aircraft during the eruption of Eyjafjallajökull in 2010," J. Geophys. Res. Atmos. **117**, D00U24 (2012).
64. J. Gasteiger, S. Groß, V. Freudenthaler, and M. Wiegner, "Volcanic ash from Iceland over Munich: mass concentration retrieved from ground-based remote sensing measurements," Atmos. Chem. Phys. **11**, 2209–2223 (2011).
65. U. Schumann, B. Weinzierl, O. Reitebuch, H. Schlager, A. Minikin, C. Forster, R. Baumann, T. Sailer, K. Graf, H. Mannstein, C. Voigt, S. Rahm, R. Simmet, M. Scheibe, M. Lichtenstern, P. Stock, H. Rüba, D. Schäuble, A. Tafferner, M. Rautenhaus, T. Gerz, H. Ziereis, M. Krautstrunk, C. Mallaun, J.-F. Gayet, K. Lieke, K. Kandler, M. Ebert, S. Weinbruch, A. Stohl, J. Gasteiger, S. Groß, V. Freudenthaler,

M. Wiegner, A. Ansmann, M. Tesche, H. Olafsson, and K. Sturm, "Airborne observations of the Eyjafjalla volcano ash cloud over Europe during air space closure in April and May 2010," Atmos. Chem. Phys. **11**, 2245–2279 (2011).
66. J. Volckens and T. M. Peters, "Counting and particle transmission efficiency of the aerodynamic particle sizer," J. Aerosol Sci. **36**, 1400–1408 (2005).
67. A. J. Armendariz and D. Leith, "Concentration measurement and counting efficiency for the aerodynamic particle sizer 3320," J. Aerosol Sci. **33**, 133–148 (2002).
68. T. M. Peters and D. Leith, "Concentration measurement and counting efficiency of the aerodynamic particle sizer 3321," J. Aerosol Sci. **34**, 627–634 (2003).
69. J. Thornburg, S. J. Cooper, and D. Leith, "Counting efficiency of the API aerosizer," J. Aerosol Sci. **30**, 479–488 (1999).
70. P. F. DeCarlo, J. G. Slowik, D. R. Worsnop, P. Davidovits, and J. L. Jimenez, "Particle morphology and density characterization by combined mobility and aerodynamic diameter measurements. Part 1: Theory," Aerosol Sci. Technol. **38**, 1185–1205 (2004).
71. L. B. Railsback, "Some fundamentals of mineralogy and geochemistry," 2006, http://www.gly.uga.edu/railsback.
72. P. Kotrappa, "Shape factors for quartz aerosol in respirable size range," J. Aerosol Sci. **2**, 353–359 (1971).
73. J. M. Alexander, D. M. Bell, D. Imre, P. D. Kleiber, V. H. Grassian, and A. Zelenyuk, "Measurement of size-dependent dynamic shape factors of quartz particles in two flow regimes," Aerosol Sci. Technol. **50**, 870–879 (2016).
74. J. G. C. Ball, B. E. Reed, R. G. Grainger, D. M. Peters, T. A. Mather, and D. M. Pyle, "Measurements of the complex refractive index of volcanic ash at 450, 546.7, and 650 nm," J. Geophys. Res. **120**, 7747–7757 (2015).